



**OPTICS, IMAGE SCIENCE, AND VISION** 

# Numerical analysis of the resolution limit in microparticle-assisted super-resolution microscopy

ARLEN R. BEKIROV,<sup>1,\*</sup> D ZENGBO WANG,<sup>2</sup> NINA A. LYSTSEVA,<sup>1</sup> BORIS S. LUK'YANCHUK,<sup>1</sup> AND ANDREY A. FEDYANIN<sup>1</sup> D

Received 15 July 2025; revised 28 August 2025; accepted 8 September 2025; posted 10 September 2025; published 1 October 2025

Visualization in the virtual image formed by dielectric microparticles has been shown to enable the distinction of objects that remain indistinguishable under direct observation. We perform the resolution analysis based on a full two-dimensional simulation in the TE mode of optical image formation, taking into account the diffraction of partially coherent light on the microparticle and the objects under study. The oscillating nature of optical resolution is demonstrated depending on the size of the microparticle. The presence of strong resonances is observed in both transmission and reflection modes. It is shown that as the size of the object decreases, the optical resolution tends to the classical limit. An analytical estimate for the resolution criterion is presented. © 2025 Optica Publishing Group. All rights, including for text and data mining (TDM), Artificial Intelligence (Al) training, and similar technologies, are reserved.

https://doi.org/10.1364/JOSAA.573559

### 1. INTRODUCTION

Examining objects with the help of dielectric microparticles allows one to resolve structures beyond the diffraction limit [1]. Various theoretical approaches have been proposed to explain this phenomenon: light focusing [2], transforming evanescent waves [3,4], resonant phenomena [5,6], source polarization [7], the effect of secondary illumination [8–10], substrate reflection [11], spatial coherence effects [12,13], and local enhancement of the numerical aperture [14]. Among them, some works are focused on modeling the propagation of radiation from a light source through the object and the microparticle up to the subsequent image formation [9,10,13,14]. In these models, the objects are not point sources but have finite dimensions. Due to computational complexity, such calculations are typically limited to the two-dimensional case. Experimental data confirm the super-resolution effect in this configuration [15]. However, the crucial question of whether a fundamental resolution limit of far-field imaging exists remains unresolved. By considering a 2D model in the TE mode, we examine the minimum achievable resolution in virtual imaging formed by microparticles and its dependence on particle size in both reflection and transmission.

Recently, we proposed a simulation method for microsphereassisted super-resolution phenomena based on the FDTD (finite-difference time-domain) approach, which demonstrated its feasibility [13]. However, this method is computationally demanding. For a monochromatic light source with wavelength  $\lambda$ , the FEM (finite element method) is more efficient and accurate. Therefore, the calculations are performed using the FEM method implemented in the MATLAB Partial Differential Equation Toolbox, utilizing the specialized "electromagnetic" class of the "harmonic" type.

# 2. RESULTS

The system under study consists of a substrate and a dielectric microcylinder with a refractive index of n=1.46. The sample is placed between the substrate and the microparticle. In the reflection mode, it consists of two rectangular metallic objects with a width of  $0.25~\lambda$ ; in the transmission mode, the structure is represented by slits of the same dimensions in a metallic screen. The system is illuminated according to the Köhler scheme. An overview of the calculation setup is shown in Fig. 1. Further details are provided in Section 4.

To determine the optical resolution, we performed a series of calculations for a fixed geometry system while varying the distance between objects. The resolution was determined using the classical bisection method.

- Define the lower and upper resolution bounds as distances S<sub>1</sub> and S<sub>2</sub>, where the objects are unresolved and resolved, respectively. By default, the resolution is assumed to be S<sub>2</sub>.
- 2. Next, we check whether the objects are distinguishable at the midpoint distance  $S_{12} = (S_1 + S_2)/2$ . If the objects are resolvable, we update the upper bound to  $S_2 = S_{12}$ ; otherwise, we set the lower bound to  $S_1 = S_{12}$ .

<sup>&</sup>lt;sup>1</sup>Faculty of Physics, Lomonosov Moscow State University, Moscow 119991, Russia

<sup>&</sup>lt;sup>2</sup>School of Computer Science and Engineering, Bangor University, Bangor, Gwynedd LL57 1UT, UK

<sup>\*</sup>bekirovar@my.msu.ru

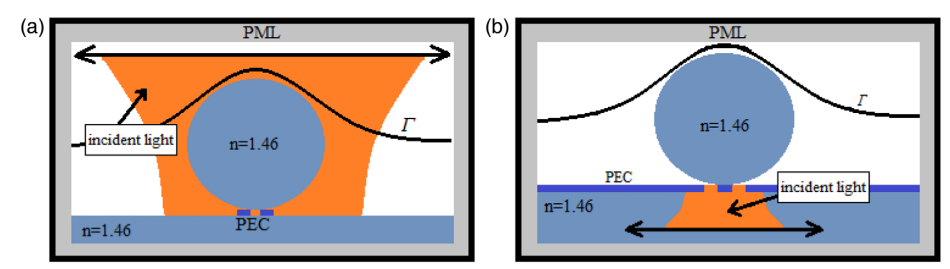


**Fig. 1.** General calculation scheme (not to scale): (a) the reflection mode, (b) the transmission mode. PEC, perfect elector conductor; PML, perfectly matched layer;  $\Gamma$  represents the wavefront reversal line for image formation.

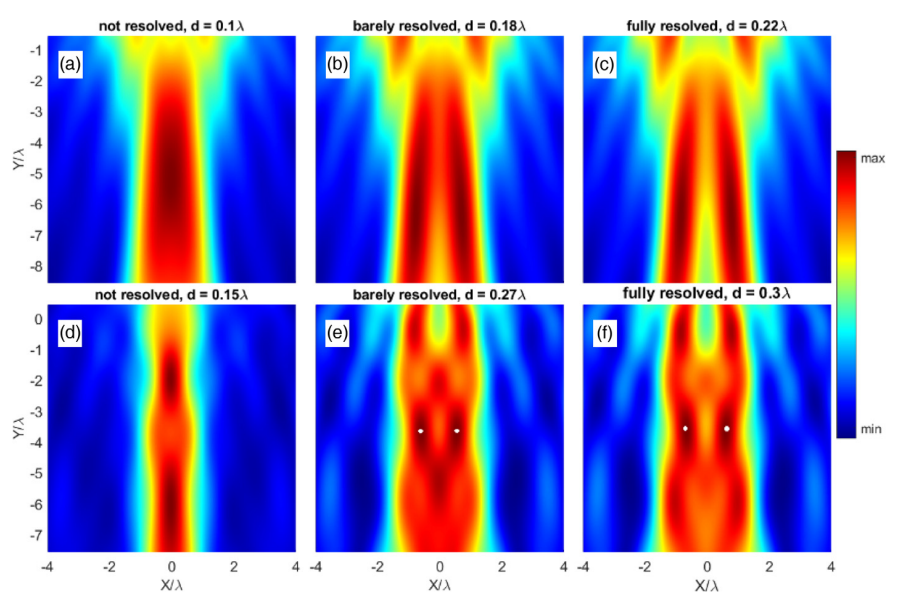


Fig. 2. Image fields for different edge-to-edge object separations d. (a)–(c) the reflection mode; (d)–(f) the transmission mode. The microparticle radius is  $R = 4.5\lambda$ . Cases (b) and (e) illustrate the minimal separation at which the objects can still be resolved. The white dots in (e) and (f) indicate the maximum field.

3. Repeat step 2 until the difference between the upper and lower bounds becomes smaller than the predefined accuracy,  $(S_2-S_1)$  <accuracy. We set the accuracy to  $0.01\lambda$ .

As the initial values, we set  $S_1=0$  and  $S_2=0.3\lambda$ . If the objects remain unresolved at  $S_2=0.3\lambda$ , the upper bound is increased by  $0.1\lambda$  until the objects become distinguishable. In Fig. 2, the image fields are presented for different edge-to-edge object separations d at a microparticle radius of  $R=4.5\lambda$ , illustrating three cases: completely unresolved, barely resolved, and fully resolved objects.

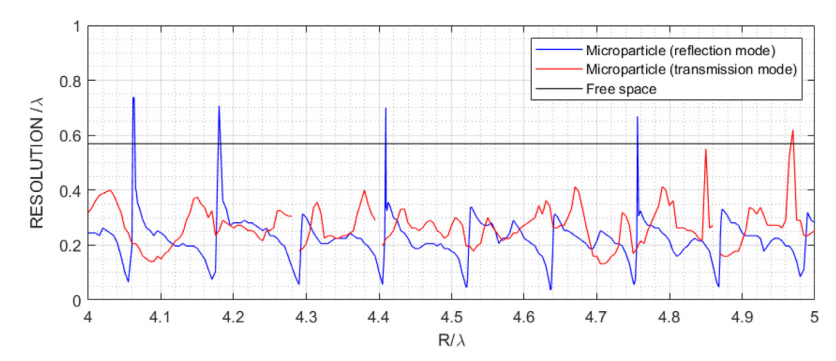
In some cases, the resolution condition is satisfied even with zero separation ( $S_2 = 0$ ), indicating that the sphere does not form an image that defines the object's geometry. In such cases, the resolution is considered indeterminate. These cases are discussed in more detail later.

Figure 3 illustrates the dependence of optical resolution on the microparticle radius R in the transmission and reflection modes. To visualize the resonance peaks, we added more calculation points for the reflection mode, while in all other cases, the calculation grid remained standard  $R=(4:0.005:5)\lambda$ . Figure 3

also shows the resolution in free space, which slightly differs from  $\lambda/2$  and is approximately  $0.55\lambda$ .

The calculations showed that the resolution in free space, i.e., in the real image, is approximately the same for both reflection and transmission geometries. However, for the virtual image, i.e., when a microparticle is present, it differs significantly. In most cases, the optical resolution surpasses the free-space limit. We also considered critical illumination. In this case, no significant changes were observed in the reflection mode, whereas in the transmission mode, the results differed considerably. Under critical illumination, the graph exhibits rapid changes, which are attributed to coherent effects.

The graphs exhibit two types of distinctive features: the areas of sharp resolution changes in Fig. 3 (reflection mode), while Fig. 3 (transmission mode) shows discontinuities. The physical origin of these features lies in the resonant field enhancement inside the particle, where the amplitude significantly increases, leading to the excitation of a whispering gallery mode. In this regime, the field inside the particle forms distinct bright maxima near its boundary [see Fig. 4(a)]. The characteristic width of these sharp resolution changes or discontinuities is approximately  $\Delta(R/\lambda) = 0.05\lambda$ .



**Fig. 3.** Dependence of the optical resolution in the virtual image on the microparticle radius R: reflection mode (red curve) and transmission mode (blue curve). The black solid lines indicate the resolution in free space without the microparticle. At the discontinuity points in the graph for the transmission mode, the resolution is undefined because the slits are distinguishable (i.e., the resolution condition is satisfied) at zero distance. The resolution in free space matches within the error margin  $(0.01\lambda)$ :  $0.57\lambda$  for the transmission mode and  $0.56\lambda$  for the reflection mode. To visualize the resonance peaks, more calculation points were added for the reflection mode.

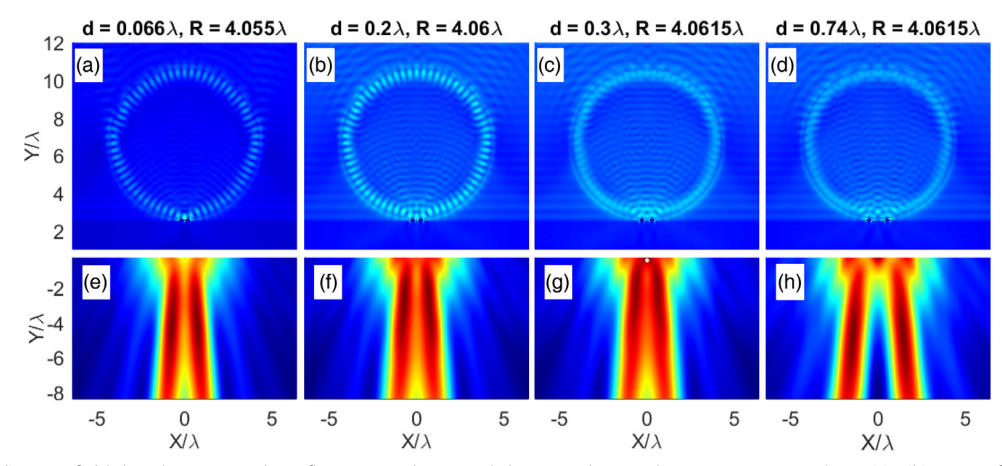


Fig. 4. (a)–(d) Near-field distributions in the reflection mode around sharp resolution changing at  $R/\lambda = 4.06$ . (e)–(h) Image fields corresponding to the cases shown in the images above. The white dot in (g) indicates the maximum field. Due to the emergence of this maximum, the optical resolution significantly deteriorates to  $0.74\lambda$ . The maximum values of the near fields for (a)–(d) are related as 1:0.6:0.6:0.6:0.6. The bright stripes at the microparticle boundary in (a) and (b) indicate the excitation of a whispering gallery mode.

Figure 4 shows the near-field distribution inside the particle and the corresponding image field near the sharp resolution changing point at  $R = 4.06\lambda$  for the reflection mode. The case of minimal resolution is illustrated in Fig. 4(a), where the formal resolution reaches an extremely small value of  $0.06\lambda$  at  $R = 4.055\lambda$ , yet exhibits significant degradation under variations in the distance between the particles. When compared to the case at  $R = 4.06\lambda$ , where the resolution is  $d = 0.2\lambda$ , the image fields appear nearly identical. Thus, at such a small resolution value, despite a threefold difference in particle separation, the distance between the maxima in the image field remains nearly unchanged. This suggests that the image field does not precisely convey the geometry and spacing of the objects but rather indicates whether one or two particles are located beneath the microsphere. Such behavior is the characteristic of the excitation of antisymmetric modes, a phenomenon noted in

The cause of the sharp resolution reduction in Figs. 4(c) and 4(d) can also be understood: it arises due to the formation of a pronounced maximum above the geometric focus. As a result,

the formal resolution condition is no longer met, even though two distinct stripes can still be observed below this maximum.

Consider the breakpoints in Fig. 3 (transmission mode). The resolution at these points is undefined because the resolution condition is satisfied even at zero distance between the slits. We found such cases only in the transmission mode. Let us examine this case in more detail using the breakpoint at  $R/\lambda = 4.4$  as an example. At first glance, it might seem that the resolution condition would continue to hold as the slit distance increases, but this is not the case. When calculated for a distance of  $d = 0.1\lambda$ , these conditions are no longer met, and this trend persists up to  $d = 0.2\lambda$ , a value that can be estimated by interpolation from the graph. Therefore, with some reservations, this value can be considered the optical resolution in this case. Figure 5 illustrates this behavior in more detail. This example highlights the need to develop more general criteria for defining optical image resolution in the presence of a microparticle.

The enhancement of the near field leads to an increased effect of secondary illumination of the sample by the field circulating inside the particle, which in turn results in the observed features. To verify this hypothesis, we performed resolution calculations,

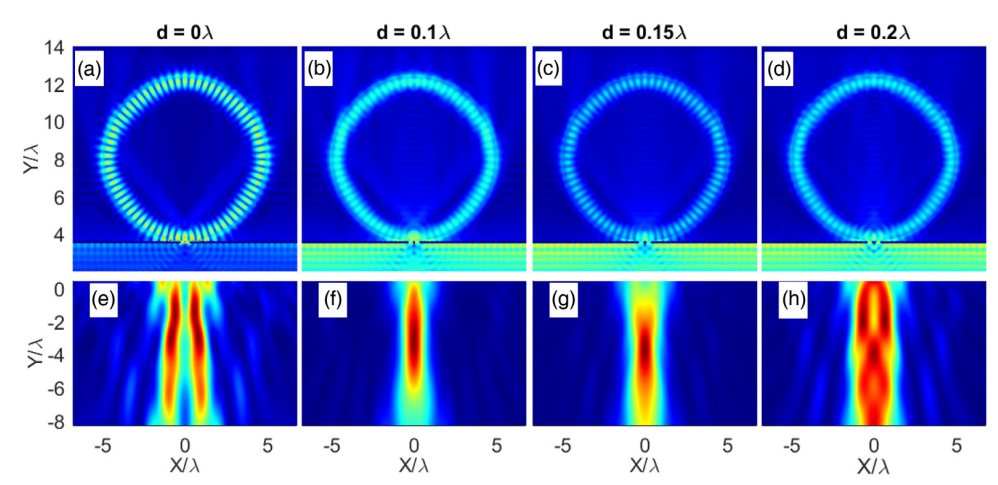
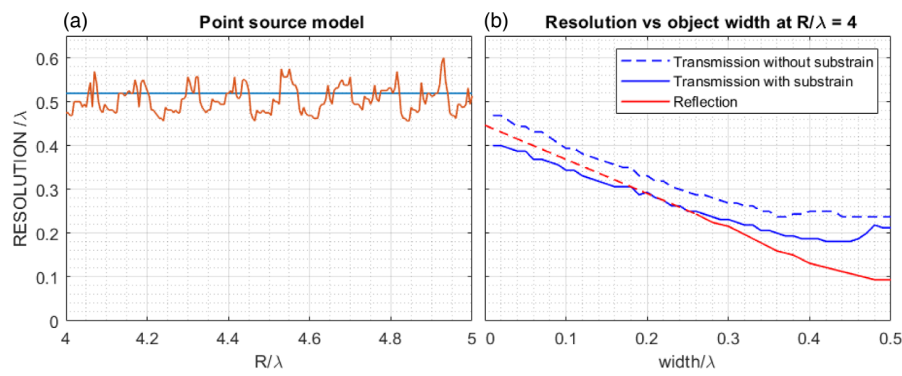


Fig. 5. (a)–(d) Near-field distributions around the slits for  $R=4.4\lambda$ , corresponding to the breakpoints in Fig. 3 (transmission mode), with slit distances  $d/\lambda=0$ , 0.1, 0.15, 0.2, respectively. (e)–(h) Image fields corresponding to the cases shown in the images above. Formal conditions for distinguishability are satisfied at  $d/\lambda=0$ ; however, in reality, the slits are distinguishable only at  $d/\lambda=0.2$ . The maximum values of the near fields for (a)–(d) are related as 1:0.4:0.4:0.4:0.4.



**Fig. 6.** (a) Dependence of the optical resolution in the point source model for free space (blue line) and in the presence of a microparticle (orange curve). The optical resolution in free space is  $0.52\lambda$ , while in the case of a microparticle, it oscillates with a small amplitude around this value. (b) Dependence of optical resolution on the object width (plates or slits) for a microparticle with  $R/\lambda = 4.4$ . The red dashed line denotes the extrapolated behavior in the limit of vanishing panel width, as direct calculation is impeded by the poor contrast of the image. The solid and dashed blue curves represent analogous dependencies in the presence and absence of a substrate beneath the slits, respectively.

where the source was modeled as two incoherent point dipoles represented as a uniformly distributed current within a cylinder with a radius of  $0.025\lambda$ . The calculation geometry and model exactly match those of the reflection mode case, meaning that we effectively replaced the reflecting objects with point sources. In this case, local field enhancement also occurs at the mentioned points; however, it does not affect the emitted field of the source. The optical resolution remains close to the theoretical limit of  $0.5\lambda$  and does not exhibit anomalies at these points, as shown in Fig. 6(a).

It should be noted that to achieve a resolution of approximately  $0.5\lambda$  in the point source model, the calculation domain was extended by  $10\lambda$  along the x axis. Otherwise, the resolution would be limited to  $0.6\lambda$ . This difference is explained by the increased numerical aperture, which enhances the collection of field information. However, this extension does not affect the results for the microsphere, as most of the rays passing through the microsphere are confined within a limited cone [14]. Moreover, only the x-component of the field was used in image calculations.

A comparison of the results in Fig. 6(a) for the point source model and those in Fig. 3 for the simulation model indicates that the key factors enabling super-resolution are the interactions between radiation and the investigated sample, as was noted to some extent in Ref. [10]. According to the presented 2D analysis, microparticle-assisted microscopy does not enhance optical resolution in terms of resolving individual point sources beyond the diffraction limit. A similar conclusion was drawn in our previous work [13], as well as in our theoretical analysis of optical resolution from the perspective of the limited number of modes excited within the microsphere [11]. This leads to the conclusion that the distinguishability of objects depends not only on the distance between them but also on their width. Figure 6(b) illustrates this dependence at  $R/\lambda = 4$ . The resolution tends to  $\lambda/2$  when object width  $\rightarrow 0$ . For object sizes smaller than  $\lambda/2$ , an approximate resolution criterion for a microparticle in the 2D case for the TE mode is given by

$$d+w pprox rac{\lambda}{2},$$
 (1)

where w is the characteristic size of the object under investigation, and d is the minimal distance (resolution value) between adjacent objects. It should be noted that this estimate is qualitative. According to the data in Fig. 3, condition (1) is satisfied with good accuracy for the average value:  $\langle d \rangle + w = 0.48 \lambda$  in the reflection mode and  $\langle d \rangle + w = 0.51\lambda$  in the transmission mode. We also note that this linear trend of resolution approaching  $\lambda/2$  is valid only outside resonant cases. For object sizes larger than  $\lambda/2$ , the optical resolution is almost independent of the object size. At  $R/\lambda = 4$ , it is approximately 0.15 $\lambda$  in the reflection mode and  $0.2\lambda$  in the transmission mode. It should be noted that these values may vary for other  $R/\lambda$  ratios. The graph in Fig. 6(b) shows an almost linear reduction of the resolution for the reflection mode as the object width decreases. Unfortunately, performing calculations for the reflection mode in the limit width  $\rightarrow$  0 was not possible due to low contrast. However, interpolation of the results suggests a resolution of  $0.44\lambda$ , which is only slightly different from the point source model, 0.47 $\lambda$ , for the same R/ $\lambda$ . In the transmission mode, when a highly conductive material is considered, this issue does not arise, and the calculations are performed down to a slit width of  $0.01\lambda$ . To ensure adequate spatial resolution for small slit widths, a mesh step of  $0.001\lambda$  was used in the slit region. However, this limiting behavior is affected by the presence of a substrate beneath the slits. Under oblique illumination, the field distribution along the lower surface of the conductor exhibits a characteristic pattern of alternating maxima and minima. Antisymmetric modes are excited when the field has a maximum near one slit and a minimum near the other, resulting in a  $\pi$  phase difference between the transmitted waves. As a result, antisymmetric mode excitation occurs, producing an image with a characteristic two-lobed pattern [16] that enables the distinction between the studied structures. Since the distance between the field lobes depends on both the angle of incidence and the refractive index of the material, the ultimate resolution is determined by the refractive index of the substrate on which the slits are placed. Consequently, the resolution limit at width  $\rightarrow$  0 in Fig. 6(b) for the transmission mode is determined by the refractive index of the substrate.

# 3. DISCUSSION

The optical resolution enabled by a microparticle depends nonlinearly on its size. This dependence may vary depending on the resolution criterion. In this study, we employ a method based on identifying the global maximum within a specified region around the geometric focus, which requires further clarification.

In the three-dimensional case, the resolvability of objects can be assessed by analyzing the intensity distribution in the focal plane. A structured intensity pattern that cannot result from random interference indicates the presence of the resolvable objects. Therefore, the focal plane should be selected to represent the geometry of the sample. In the two-dimensional case, with a fixed observation plane, only a one-dimensional field distribution  $\mathbf{E}^{\text{im}}(x)$  can be recorded, making it challenging to directly correlate the observed intensity dip between maxima with the sample's geometry. If the geometry of the sample is known *a priori*, the focal line  $y=y^{\text{image}}$  can be chosen to optimally represent its structure. However, in microscopy, where the

goal is to investigate unknown objects with an undetermined geometry, such an approach is not applicable.

For example, depending on the choice of  $y^{\text{image}}$ , the sample may be interpreted either as a single slit or as two separate slits. The global maximum search eliminates this ambiguity. Furthermore, the definition of the optical resolution limit implies that if the distance between objects exceeds this threshold, they must remain distinguishable. If the focal plane is selected outside the global maximum, this condition may not be satisfied.

An alternative approach is to assess resolution at a fixed position of  $y^{\text{image}}$ , for example, in the region of the geometric focus. However, due to significant aberrations introduced by the microparticle, which cause all rays to converge at a single point, this choice becomes somewhat arbitrary. In this study, we aim to establish a resolution criterion that is both objective and robust.

Equation (1), which provides an estimate of the resolution limit, applies to the two-dimensional case in the TE mode; its validity in three dimensions has not been demonstrated so far. The quantitative values can differ significantly between the 2D and 3D cases. To confirm this result for the 3D case, one would need to perform calculations similar to those shown in Fig. 6(b), which is computationally challenging. The present work is limited to 2D simulations; however, the presented model can be directly extended to the 3D case. Thus, this study lays the groundwork for future research.

#### 4. MATERIALS AND METHODS

#### A. Image Field Calculation Approaches

There are several methods in the literature for calculating the image field at micrometer scales. In this section, we briefly describe them for the two-dimensional case. Let the field  ${\bf E}$  be generated by a certain coherent monochromatic source, which we will refer to as the source field. The temporal dependence takes the form  $\sim e^{-i\omega t}$ , which we will omit unless stated otherwise. The source field can be associated with its corresponding image field  ${\bf E}^{\rm im}$  according to the following formula:

$$\mathbf{E}^{\mathrm{im}}(r_0) = \frac{-i}{4} \int_{\Gamma} \left[ G(\mathbf{n}, \nabla) \mathbf{E}^* - \mathbf{E}^*(\mathbf{n}, \nabla) G \right] \mathrm{d}l, \quad (2)$$

where  $\Gamma$  is an arbitrary curve homotopic to an infinite line,  $G = H_0^{(1)}(k|r-r_0|)$  is the Hankel function of the first kind, and \* denotes complex conjugation,  $k = 2\pi/\lambda$ ,  $\nabla = \partial/\partial \mathbf{r}$ , and  $\lambda$  is the wavelength. The complex conjugation of the source field reverses the wave front, transforming the field from diverging to converging to the source. Equation (2) can be rewritten in Fourier space as follows:

$$\mathbf{E}^{\text{im}}(r_0) = \frac{1}{2\pi k} \int_{-k}^{k} \tilde{\mathbf{E}}^*(k_x, y_0) e^{-i(k_x x - k_y (y - y_0))} dk_x, \quad (3)$$

where  $\tilde{\mathbf{E}}$  is the Fourier transform of the field  $\mathbf{E}$  at  $y = y_0$ , and  $k_y = \sqrt{k^2 - k_x^2}$ . According to Eq. (3) and in accordance with Abbe's definition, the image field does not contain evanescent harmonics with  $k_y > k$ .

In the case when the source field is generated by scattering on a microparticle, the fields  $\mathbf{E}^{\mathrm{im}}$  and  $\mathbf{E}$  can be expanded in terms of cylindrical functions. For the TM geometry ( $E_x = E_y = 0$ ),

these expansions take the following form [17]:

$$\mathbf{E} = \sum_{l=-\infty}^{\infty} a_l \mathbf{N}_l,$$

$$\mathbf{E}^{\mathrm{im}} = \sum_{l=-\infty}^{\infty} a_l^{\mathrm{im}} R g \mathbf{N}_l^*.$$
 (4)

For convenience, the field  $\mathbf{E}^{\mathrm{im}}$  is expanded using complex-conjugated functions,  $\mathbf{N}_l = e^{il\varphi} H_l^{(1)}(k\rho)\mathbf{e}_z$ ,  $H_l^{(1)}$  is the Hankel function of the first kind, and Rg denotes the extraction of the regular part of the expression. Due to the linearity of Eqs. (2) and (3), the column vectors of the expansion coefficients of the source field  $(a_l)$  and the image field  $(a_l^{\mathrm{im}})$  are related by a matrix equation of the form

$$\begin{pmatrix} \dots \\ a_{-1}^{\text{im}} \\ a_{0}^{\text{im}} \\ a_{1}^{\text{im}} \\ \dots \end{pmatrix} = \mathbf{A}^{\text{im}} \begin{pmatrix} \dots \\ a_{-1}^{*} \\ a_{0}^{*} \\ a_{1}^{*} \\ \dots \end{pmatrix}. \tag{5}$$

The components of the matrix  $\mathbf{A}^{\text{im}}$ , which link the coefficient  $a_n$  on the right-hand side with the coefficient  $a_m^{\text{im}}$  on the left-hand side of the expression, are given by  $(A^{\text{im}})_{nm} = \text{sinc}((n-m)/2)$ . This operator was first computed for the three-dimensional case in Ref. [11]. In the two-dimensional case, the calculations are analogous; for more details, see Supplement 1.

For the TE geometry ( $E_z=0$ ), the fields **E** and **E**<sup>im</sup> can be similarly expanded using functions  $\mathbf{M}=\operatorname{rot}(\mathbf{N})/k$ . Due to the linearity of this transformation, Eq. (5) and the components of the matrix  $\mathbf{A}^{\text{im}}$  remain unchanged.

If the source field is non-stationary,  $\mathbf{E} = \mathbf{E}(t)$ , there are two approaches to compute the corresponding time dependence of  $\mathbf{E}^{\mathrm{im}}(t)$ . In the first approach, the time dependence can be expanded into a Fourier series. Then, by applying transformations [Eqs. (2)–(3)] to each component and performing an inverse Fourier transform, the dependence  $\mathbf{E}^{\mathrm{im}}(t)$  can be obtained.

The second approach involves the FDTD (finite-difference time-domain) method [13]. In this method, the field sources are explicitly defined at the grid nodes, and the field propagation in space is computed using a finite-difference scheme in the time domain. To ensure that the generated pulse corresponds to the image field rather than the source field, the time dependence must be reversed.

For the TM geometry, the setup of sources for generating the image field is implemented as follows:

$$\begin{split} &E_z^{\text{im}}(x, y = y_o, t + dt) \\ &= E_z^{\text{im}}(x, y = y_o, t) + (E_z(x, y = y_o + dy, -t) \\ &- E_z(x, y = y_o, -t))/dy + E_z(x, y = y_o, -t)/dy, \quad \textbf{(6)} \\ &E_z^{\text{im}}(x, y = y_o + dy, t + dt) \\ &= E_z^{\text{im}}(x, y = y_o + dy, t) - E_z(x, y = y_o, -t)/dy, \quad \textbf{(7)} \end{split}$$

where  $y = y_0$  is the line on which the sources are defined, and dt and dy are the time and spatial grid steps, respectively. A similar approach can be applied in the TE geometry for each component  $E_x$ ,  $E_y$ , or by defining the source through the magnetic component  $H_z$ .

In our calculations, we used the FEM method, which allows us to obtain the spatial distribution of the source field. For this reason, we applied Eq. (2). The curve  $\Gamma$  was chosen as a smooth, bell-shaped contour enclosing both the particle and the surrounding space. Such a configuration captures all rays emanating from the microsphere. If  $\Gamma$  is chosen as a straight line, achieving the same result would require the line to be significantly larger than the microsphere's diameter, substantially increasing the simulation domain. Similar optimizations were performed in Ref. [9].

#### **B.** Calculation Setup

For accurate calculations, the mesh size in the source generation and object regions must be especially fine. The maximum distance between mesh nodes was set to  $0.066\lambda$ , with further refinement in the specified regions to  $0.005\lambda$ . Simulations were conducted for microsphere sizes  $R = (4:0.005:5)\lambda$  with a refractive index of n = 1.46.

In the reflection geometry, the sample was composed of rectangular perfect conductors with a width of  $0.25\lambda$  and a height of  $0.1\lambda$ . For the transmission geometry, the sample was represented by slits in an opaque screen of the same dimensions. The entire structure was placed on a substrate with a refractive index of n = 1.46.

The dimensions of the simulated region were  $(4.4R + 8\lambda) \times (2R + 5.9\lambda)$ . If the contact point between the microparticle and the substrate is taken as the origin, the curve  $\Gamma$  is defined by the following equation:

$$y = 3\lambda + (2R + 0.2\lambda) \left( 1 + \left( \frac{x}{1.2R} \right)^4 \right)^{-1}$$
.

This dependence ensures a  $3\lambda$  offset from the substrate surface to avoid edge effects.

To ensure a physically accurate assessment of the resolution, it is crucial to define the illumination conditions properly. In the calculations, we used the Köhler illumination scheme, where the sample is illuminated by incoherent plane waves at various incident angles. Plane-wave illumination is confined within a cone with a half-angle of  $3\pi/8$  (NA = 0.92), with an angular step of  $\pi/100$ , for both transmission and reflection geometries.

Figure 7 shows the near-field and the corresponding image field in the absence of a microparticle at different object separation distances. The figure illustrates two representative scenarios: zero spacing between adjacent object elements and the minimal separation distance at which the object features remain just resolvable.

# C. Image Formation Algorithm by an Incoherent Source and the Criterion of Resolution

The algorithm for calculating the image field for a spatially incoherent source includes the following key steps: computing the image field for a specific plane-wave incidence angle, varying

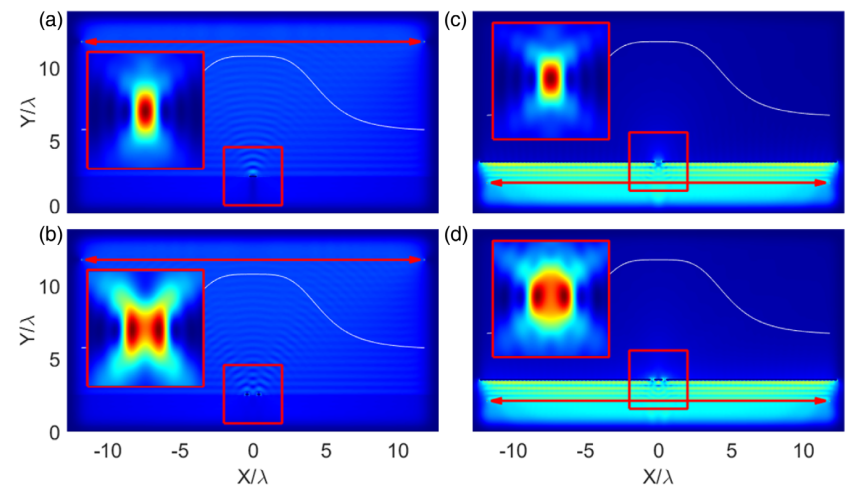


**Fig. 7.** Real and image fields without a microsphere. The white curve represents the integration path  $\Gamma$ , and the red double arrow line represents the source injection line. The insets display the image field calculated for the area highlighted by the red square. (a), (b) The reflection mode, with distances between objects d=0 and  $d=0.56\lambda$ , respectively. (c), (d) The transmission mode, with distances between apertures d=0 and  $d=0.57\lambda$ , respectively.

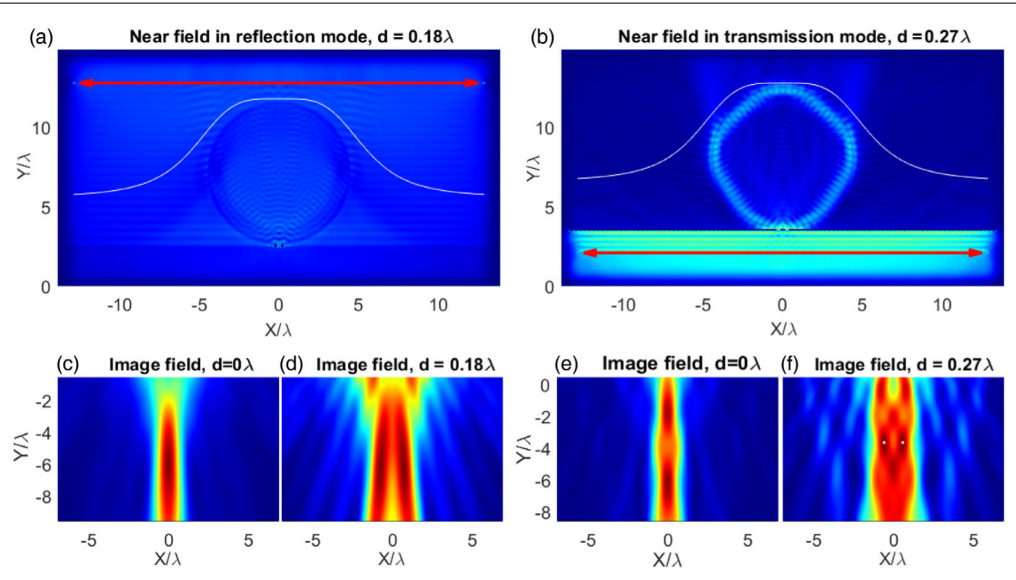


**Fig. 8.** (a), (b) Near-field distribution in the reflection and transmission modes, respectively. Image field in the reflection mode with object separation of  $d = 0\lambda$  (c),  $d = 0.18\lambda$  (d). Image field in the transmission mode with a slit separation of  $d = 0\lambda$  (e),  $d = 0.27\lambda$  (f). The white dots in (f) indicate the maximum field. The particle radius is  $R = 4.5\lambda$ , n = 1.46. The white curve represents the integration path  $\Gamma$ , and the red double arrow line represents the source injection line.

the angle of incidence, and summing the intensity contributions from all angles. The image field is computed using Eq. (2) in a rectangular area centered at the geometric image position, determined by the magnification formula n/(2-n)R, with dimensions  $(2.2R+4)\times 2R$ .

The resolution condition is defined as follows: let the maximum of the image intensity field distribution for x>0 be at point  $A_1$ , and for x<0 at point  $A_2$ . The objects are considered resolvable if the intensity at the midpoint  $A_{12}$  exhibits an 80% dip relative to the maxima at  $A_1$  and  $A_2$  points.

In many cases, due to overlapping image fields from each object, the maximum shifts toward the center, forming a single peak above or below two distinct local maxima. If this central

maximum is excluded, the resolution criterion is satisfied, and the objects (e.g., slits) can be considered resolvable. However, such cases are not considered in the presented calculations, meaning that the optical resolution is estimated conservatively, or "from below."

Figure 8 shows the near-field and the corresponding image field for a microparticle with  $R=4.5\lambda$  at different object distances. The microparticle does not generate an image in the same manner as in free space. In the case of a microcylinder, the image appears as elongated bright stripes, whereas in free space, the image is localized on a wavelength scale, as evident from the comparison between Figs. 7 and 8.

**Funding.** Foundation for the Advancement of Theoretical Physics and Mathematics (23-1-1-61); Bangor University (BUIIA-S46910); Royal Society (IEC\R2\202178); Leverhulme Trust (RF-2022-659).

**Acknowledgment.** The study was carried out within the framework of the state assignment of the Lomonosov Moscow State University; the work was also supported by a grant from the Foundation for the Development of Theoretical Physics and Mathematics "BASIS" (grant No. 23-1-1-61). Z.W. is thankful for support from the Leverhulme Trust (RF-2022-659), the Royal Society (IEC\R2\202178), and Bangor University (BUIIA-S46910).

**Disclosures.** The authors declare no conflicts of interest.

**Data availability.** Data are available upon reasonable request.

**Supplemental document.** See Supplement 1 for supporting content.

#### **REFERENCES**

- Z. Wang, W. Guo, L. Li, et al., "Optical virtual imaging at 50 nm lateral resolution with a white-light nanoscope," Nat. Commun. 2, 218 (2011).
- H. Yang, R. Trouillon, G. Huszka, et al., "Super-resolution imaging of a dielectric microsphere is governed by the waist of its photonic nanojet," Nano Lett. 16, 4862–4870 (2016).
- R. Boudoukha, S. Perrin, A. Demagh, et al., "Near- to far-field coupling of evanescent waves by glass microspheres," Photonics 8, 73 (2021).
- S. Lee, L. Li, Y. Ben-Aryeh, et al., "Overcoming the diffraction limit induced by microsphere optical nanoscopy," J. Opt. 15, 125710 (2013)
- Y. Duan, G. Barbastathis, and B. Zhang, "Classical imaging theory of a microlens with super-resolution," Opt. Lett. 38, 2988–2990 (2013).

- A. Bekirov, B. Luk'yanchuk, and A. Fedyanin, "Virtual image within a transparent dielectric sphere," JETP Lett. 112, 341–345 (2020).
- C. Simovski and H. Reza, "A simple glass microsphere may put the end to the metamaterial superlens story," AIP Conf. Proc. 2300, 020117 (2020).
- V. Astratov, Y. Sahel, Y. Eldar, et al., "Roadmap on label-free superresolution imaging," Laser Photonics Rev. 17, 2200029 (2023).
- A. Maslov, "Effect of boundary conditions in modeling of microsphere-assisted imaging," Appl. Opt. 63, 4372–4379 (2024).
- A. Maslov and V. Astratov, "Origin of the super-resolution of microsphere-assisted imaging," Appl. Phys. Lett. 124, 061105 (2024).
- A. Bekirov, "On superresolution in virtual image in a transparent dielectric sphere," Opt. Spectrosc. 131, 363–369 (2023).
- A. Bekirov, B. Luk'yanchuk, Z. Wang, et al., "Wave theory of virtual image," Opt. Mater. Express 11, 3646–3655 (2021).
- A. Bekirov, B. Luk'yanchuk, Z. Wang, et al., "Dielectric microparticles for enhanced optical imaging: an FDTD analysis of contrast and resolution," J. Opt. Soc. Am. A 42, 45–50 (2025).
- T. Pahl, L. Hüser, S. Hagemeier, et al., "FEM-based modeling of microsphere-enhanced interferometry," Light Adv. Manuf. 3, 699–711 (2022).
- K. Allen, N. Farahi, Y. Li, et al., "Overcoming the diffraction limit of imaging nanoplasmonic arrays by microspheres and microfibers," Opt. Express 23, 24484–24496 (2015).
- A. V. Maslov and V. N. Astratov, "Imaging of sub-wavelength structures radiating coherently near microspheres," Appl. Phys. Lett. 108, 051104 (2016).
- W. Sun, N. G. Loeb, and B. Lin, "Light scattering by an infinite circular cylinder immersed in an absorbing medium," Appl. Opt. 44, 2338–2342 (2005).